

# Computational Models of Laryngeal Aerodynamics: Potentials and Numerical Costs

\*Hossein Sadeghi, \*Stefan Kniesburges, †Manfred Kaltenbacher, \*Anne Schützenberger, and \*Michael Döllinger, \*Erlangen, Germany, and †Vienna, Austria

**Summary:** Human phonation is based on the interaction between tracheal airflow and laryngeal dynamics. This fluid-structure interaction is based on the energy exchange between airflow and vocal folds. Major challenges in analyzing the phonatory process in-vivo are the small dimensions and the poor accessibility of the region of interest. For improved analysis of the phonatory process, numerical simulations of the airflow and the vocal fold dynamics have been suggested. Even though most of the models reproduced the phonatory process fairly well, development of comprehensive larynx models is still a subject of research. In the context of clinical application, physiological accuracy and computational model efficiency are of great interest. In this study, a simple numerical larynx model is introduced that incorporates the laryngeal fluid flow. It is based on a synthetic experimental model with silicone vocal folds. The degree of realism was successively increased in separate computational models and each model was simulated for 10 oscillation cycles. Results show that relevant features of the laryngeal flow field, such as glottal jet deflection, develop even when applying rather simple static models with oscillating flow rates. Including further phonatory components such as vocal fold motion, mucosal wave propagation, and ventricular folds, the simulations show phonatory key features like intraglottal flow separation and increased flow rate in presence of ventricular folds. The simulation time on 100 CPU cores ranged between 25 and 290 hours, currently restricting clinical application of these models. Nevertheless, results show high potential of numerical simulations for better understanding of phonatory process.

**Key Words:** Human phonation–Numerical larynx model–Glottal aerodynamics–Large eddy simulation–Computational cost.

## INTRODUCTION

In engineering disciplines, computational software packages for simulating fluid flow and structural dynamics have been established as standard tools in the development process of innovative products. These software tools provide great advantages: fast and cheap analysis of prototypes or innovative processes without the construction of physical models, separate analysis of influencing aspects, and high spatial and temporal resolutions of the results with almost unconfined access to the simulated region.

Voice research with a focus on the physical process of sound generation suffers from the highly restricted region of interest (ROI).<sup>1</sup> The ROI contains the subglottal region, the glottal region with the vocal folds, and the supraglottal region. Moreover, the vocal tract, consisting of the pharynx and the upper airways, is also highly restricted for positioning sensors to analyze the fluid flow and the acoustic field. Therefore, computational models based on continuum mechanics possess high potential regarding the analysis of the phonatory process. In addition to basic research, the ultimate goal is the development of numerical tools in phonosurgery with the aim of estimating postsurgical outcome in advance.<sup>2</sup>

Computational larynx models can be categorized in two general groups: (1) static vocal fold models and (2) moving vocal fold models. The second group is further subdivided into those with externally forced or flow-induced self-sustained oscillating vocal folds. Among all of the studies mentioned here, 23 (31.5%) used static models of vocal folds,<sup>3–25</sup> 19 (26%) employed forced oscillation,<sup>26–44</sup> and 31 (42.5%) produced self-sustained oscillations of vocal folds by considering the coupled fluid-structure interaction.<sup>45–75</sup>

Static models exhibit fixed and rigid vocal folds forming a glottal duct shape corresponding to specific instances in the oscillation cycle: convergent shape for the glottis opening and divergent shape for its closing motion. This approach is based on the quasi-steady assumption of the glottal flow.<sup>76</sup> It describes the dynamic glottal flow field as a series of steady and fully developed flow fields between rigid vocal folds with geometric and aerodynamic conditions of corresponding instances during the oscillation cycle of elastic vocal folds. The major aim of static vocal fold models is the investigation of glottal aerodynamics. Previous studies focused on the influence of different glottal shapes<sup>7–10</sup> and the presence of ventricular folds (VeFs)<sup>17–22</sup> on the glottal and especially the supraglottal flow field downstream of the vocal folds that exhibits the glottal jet.<sup>13–16</sup> Furthermore, first attempts to simulate sound generation on the basis of acoustic analogies have been made.<sup>23–25</sup>

In the group of dynamic models with externally driven vocal folds, the shape of the glottal duct is varied according to the ideal patterns of vocal fold motion<sup>26–28</sup> adapted from experiments<sup>29,40</sup> or simulations with elastic vocal folds.<sup>30</sup> The great advantage of this approach is the reduction of the physical problem to a pure simulation of the fluid dynamics with moving boundary walls forming the glottal duct. Beside relatively simple one-dimensional

Accepted for publication January 4, 2018.

From the \*Division of Phoniatrics and Pediatric Audiology at the Department of Otorhinolaryngology, Head and Neck Surgery, University Hospital Erlangen, Medical School at Friedrich-Alexander University Erlangen-Nürnberg, Erlangen, Germany; and the †Institute of Mechanics and Mechatronics, TU Wien, Vienna, Austria.

Address correspondence and reprint requests to Hossein Sadeghi, Division of Phoniatrics and Pediatric Audiology at the Department of Otorhinolaryngology, Head and Neck Surgery, University Hospital Erlangen, Medical School at Friedrich-Alexander University Erlangen-Nürnberg, Waldstraße 1, 91054, Erlangen, Germany. E-mail: [hossein.sadeghi@uk-erlangen.de](mailto:hossein.sadeghi@uk-erlangen.de)

Journal of Voice, Vol. ■■■, No. ■■■, pp. ■■■–■■■  
0892-1997

© 2018 The Voice Foundation. Published by Elsevier Inc. All rights reserved.

<https://doi.org/10.1016/j.jvoice.2018.01.001>

dynamics of the vocal folds with only transversal motion,<sup>31</sup> more complex two-dimensional (2D) and three-dimensional (3D) dynamics<sup>32,33</sup> have been applied, mimicking convergent-divergent shape changes of the glottal duct and a realistic elliptical (ELL) glottis shape. This type of numerical larynx models was mostly used to study the aerodynamics as a result of varying geometric conditions due to the vocal fold motions. These models successfully reproduced glottal flow characteristics such as the location of the separation point of the glottal jet, the pressure distribution along the glottal duct, the asymmetric glottal jet location in the supraglottal region, and the flow resistance.<sup>26,28,32,34</sup> With the application of dynamic vocal fold models, the analysis of the sound generation came into focus because of the periodical characteristics of the flow field.<sup>35,36</sup> In this context, the main concern was with the basic mechanisms of sound production during phonation and the influence of different vocal fold oscillation patterns<sup>37-41</sup> and the choice of compressible or incompressible flow models for the glottal flow simulation.<sup>42-44</sup> With those larynx models, acoustic source distribution in glottal and supraglottal flow fields was determined, which coincided with experimental findings.<sup>77,78</sup>

However, besides all of the advances, larynx models with externally driven vocal folds do not include the interaction between flow and vocal fold tissue. As a consequence, the response of the vocal folds on the flow and the resulting tension distribution in the tissue are not reproduced and therefore cannot be evaluated. Nevertheless, on the condition that the vocal fold motion is explicitly known in detail, these models with externally driven vocal folds are able to reproduce the entire process of sound generation.

The third and most complex type of simulation in this field is the simulation of the complete fluid-structure interaction, including computational structural mechanics. By this approach, flow-induced self-sustained oscillations of vocal folds have been achieved in 2D<sup>45-48</sup> and 3D models.<sup>49-52</sup> In addition to the aim of gaining a fundamental understanding of phonation, first attempts on simulating vocal fold pathologies such as tension imbalance between both vocal folds due to unilateral paralysis<sup>53,54</sup> or subglottal stenosis<sup>55</sup> were made. However, most studies focused on the development of adequate numerical models and methods for the simulation of the fully coupled process of fluid-structure interaction. A special interest was in the morphologic structure of the vocal folds. Vocal fold models consisting of one up to four layers with different material properties have been applied.<sup>56-60</sup> Furthermore, the choice of an appropriate material model for the tissue is critical because of the inhomogeneous and anisotropic morphology of vocal fold tissue.<sup>79</sup> Relatively simple material models, such as the linear elasticity model following the Hooke law, and also more complex nonlinear viscoelastic or hyperelastic models have been applied.<sup>58-61,80</sup> As a consequence, a clinical application of those fully coupled models is very critical. For obtaining clinically relevant information on a patient's phonation, these models would require not only an extremely large amount of computational power but also the exact determination of instantaneous material properties of the vocal fold tissue during the patient's spontaneous phonation. Only with this information could the computational model reproduce the individual

phonation process with appropriate accuracy. Therefore, fully coupled vocal fold models have large potentials in the scientific development of material models for the vocal fold tissue. However, for the acoustic analysis of phonation, models with externally driven vocal fold motion exhibit the entire physical process of sound generation.

To create numerical larynx models based on continuum mechanics, the ROIs have to be discretized in space and time. Depending on the type of model, these regions include the flow region only (first and second types) or additionally the volume of the vocal folds for simulating the fully coupled fluid-structure interaction (third type). In principle, three numerical methods are commonly applied in commercial and scientific simulation tools:

- Finite difference method (FDM)
- Finite volume method (FVM)
- Finite element method (FEM)

Whereas the finite difference method and FVM are mainly used in computational fluid dynamics, the finite element method has been applied more in computational structural mechanics and aeroacoustics. In all three methods, the region or volume of interest is divided into small control elements (finite 2D surface or 3D volume). Subsequently, the governing equations for the particular physical problem (fluid dynamics, structural dynamics, and acoustics) are discretized and solved for each control element in relation to its boundary conditions according to the surrounding neighboring elements. The governing equations are the Navier-Stokes equations for fluid flow,<sup>81</sup> the Navier-Lame equations for structural dynamics (mostly applied in combinations with the linear elasticity material model), and the wave equation for acoustics.<sup>82</sup> For simulating the fully coupled fluid-structure interaction between glottal flow and vocal folds, two numerical methods have been applied in voice research: (1) the arbitrary Lagrangian-Eulerian (ALE)<sup>83</sup> and (2) the immersed boundary method.<sup>84</sup>

Despite all the advantages that numerical models provide, the computational costs for the simulations are high. In principle, numerical costs represent the temporal and technical (hardware of computer system) effort that has to be expended for performing meaningful simulations. Unfortunately, only a small proportion (~25%) of published studies provides detailed information on numerical costs. Table 1 presents a summary of studies that provided data on computational costs. The costs are represented by the CPU time and the wall time that indicate the time summed over all processors and the overall real time needed for performing the simulation, respectively.

The computational cost usually increased with the complexity of the simulations and the size of the mesh. It ranges from some hours in early studies with static vocal folds and low mesh resolutions to several weeks employing very powerful supercomputers for fully coupled simulations with high mesh resolutions. However, most studies did not provide all information on the numerical effort. As a consequence, it is difficult to examine the potential of these tools, especially in clinical application.

TABLE 1.

**Computational Costs of Previous Studies Including simulated Motion of Vocal Folds, Dimensionality of the Problem, Method of Discretization, and Mesh Population**

	Motion	D	Method	Cells	Cycles	Cores/clock rate	CPU Time (h)	Wall Time (h)
Iijima et al <sup>4</sup>	Static	2D	FEM	4k	—	1/-	3–4	—
Guo and Scherer <sup>5</sup>	Static	2D	FEM	630	—	1/11.12 MHz	3	—
Alipour et al <sup>26</sup>	Forced motion	2D	FVM	6k	1	1/174 MHz	—	4.5
Renotte et al <sup>85</sup>	Forced motion	3D	FVM	72.8k	1	1/-	—	3–4
Zheng et al <sup>31</sup>	Forced motion	2D	IBM	131k	20	4/3 GHz	2,000	—
Šidlof and Zörner <sup>39</sup>	Forced motion	3D	FVM	2.1M	20	16/-	—	245
Šidlof et al <sup>36</sup>	Forced motion	3D	FVM	2.1M	20	16/-	—	245
Šidlof et al <sup>38</sup>	Forced motion	3D	FVM	2.4M	20	—	3,900 core-h	—
Šidlof et al <sup>41</sup>	Forced motion	3D	FVM	2.4M	20	—	4,600 core-h	—
Zörner et al <sup>37</sup>	Forced motion	3D	FVM	0.5–1.5	20	24/-	—	384
Duncan et al <sup>56</sup>	Self-sustained	2D	PBI	1M, 34k	4.6	—	—	O(wk)
Luo et al <sup>45</sup>	Self-sustained	2D	IBM	73k, 5k	1	1/1.8 GHz	15	—
Link et al <sup>47</sup>	Self-sustained	2D	FEM	22.8k, 3k	1	8/3 GHz	—	10
Pickup and Thomson <sup>59</sup>	Self-sustained	2D	FEM	19k, 3k	3.5	4/2.8 GHz	—	19
Xue et al <sup>62</sup>	Self-sustained	2D	IBM	83k, 200	10	1/2 GHz	300–500	—
Zheng et al <sup>63</sup>	Self-sustained	3D	IBM	2.1M, 58k	1	128/2.66 GHz	—	45
Zheng et al <sup>64</sup>	Self-sustained	3D	IBM	2.1M, 58.4k	21	128/3 GHz	90,000	720
Xue et al <sup>53</sup>	Self-sustained	3D	IBM	2.1M, 126.2k	30	128/3 GHz	—	1,200
Xue et al <sup>54</sup>	Self-sustained	3D	IBM	2.1M, 126.2k	30	128/3 GHz	—	1,200
Xue et al <sup>50</sup>	Self-sustained	3D	IBM	2.1M, 47.9k	8	512/3 GHz	30,720	240
Jo et al <sup>52</sup>	Self-sustained	3D	FDM	427.9k	—	8/-	—	O(wk)

Abbreviation: D, dimensional.

Hence, the aim of the present study was to simulate the aerodynamics of the human phonation process with the commercial software package *STAR-CCM+* (Siemens PLM software, Plano, TX/USA) and to evaluate the computational costs as a function of the degree of realism. With regard to the potential clinical application of computational models, flow simulations were carried out with static or externally driven vocal fold oscillations. Models with flow-induced vocal fold oscillations were excluded because of the large requirement of computational power and the lack of diagnostic techniques for determining the material properties of the vocal fold tissue during a patient's phonation. For presenting the total extent of the numerical modeling approach, the mesh independence study is described in detail additionally to the aerodynamic results and the numerical costs.

The computational larynx model is based on a synthetic experimental larynx model being described in the literature<sup>77,86–89</sup> and being similar to synthetic models applied elsewhere.<sup>58,90,91</sup>

## LARYNX MODEL AND NUMERICAL METHODS

### Geometric dimensions

The numerical larynx model is based on an experimental synthetic larynx model.<sup>77,86–88</sup> The geometric dimensions of the numerical flow domain and the vocal fold models are on the human length scale. A schematic of the numerical model is displayed in Figure 1.

The numerical model is divided into the subglottal part upstream of the vocal folds, the glottal duct with the vocal folds,

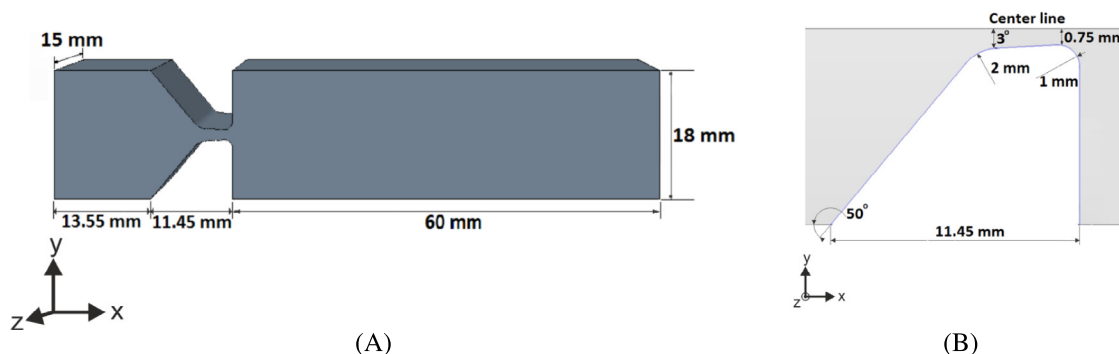


**FIGURE 1.** (A) Geometry of the numerical larynx model: subglottal, glottal, and supraglottal regions. (B) Geometry of vocal folds in a coronal cut according to the M5 model.<sup>58,92</sup>

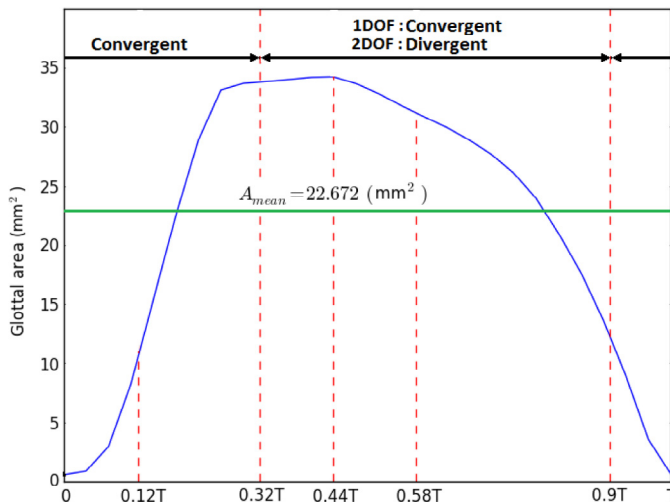


**FIGURE 2.** Glottal area and motion of the vocal folds as derived from the experimental model.<sup>77,93</sup>

and the supraglottal part downstream of the vocal folds. The sub- and supraglottal parts have a rectangular cross section of  $18 \times 15$  mm and a length of 13.55 and 60.0 mm, respectively. For capturing the whole glottal jet, the length of the supraglottal part was selected based on experimental results.<sup>77,87</sup> The shape of the vocal folds corresponds to the simplified M5 model proposed by Thomson et al and Scherer et al.<sup>58,92</sup>

In our work, the vocal folds were static or externally driven to model the periodic oscillations of the vocal folds. The motion of the vocal folds was prescribed by moving the wall boundaries that form the glottal duct by the vocal folds. In the case of static vocal folds, the rectangular glottis area is defined as the mean glottal area obtained from the experimental model<sup>93</sup> with a glottal gap diameter of 1.5 mm. For the externally driven vocal fold motion, the time-varying glottal gap has either a rectangular or an ELL shape. The glottal gap diameter was derived from the corresponding glottal area as measured in the experimental model. Figure 2 shows the glottal area waveform for one oscillation cycle of the vocal folds and its average adapted from the experimental model.<sup>93</sup>

Five different cases of vocal fold dynamics were simulated with an increasing degree of realism. With this approach, we want to evaluate the potentials of numerical simulations regarding scientific and clinical relevant information. Also, the present study will show which model details might be negligible or important for studying certain phonatory aspects. Further, the computational costs will be discussed. In addition to the static

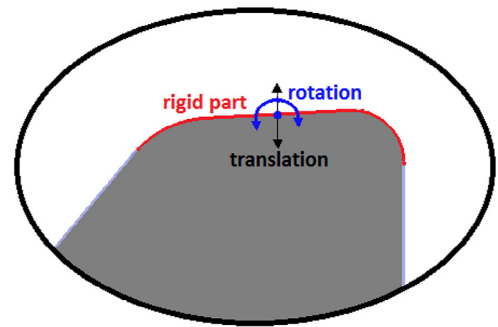


**FIGURE 3.** Rigid part of the vocal fold in addition to the translational and rotational motions. (For interpretation of the references to color in this figure legend, the reader is referred to the Web version of this article.)

vocal fold case, four cases with externally driven vocal fold motions were applied: one case with one degree of freedom (1DOF) motion and three cases with two degrees of freedom (2DOF) motion. Except for the last case, which had an ELL glottis shape, all cases possessed a rectangular glottal area. A summary of all cases with the relevant parameters is given in Table 2.

For the 1DOF motion, the vocal folds moved only transversally in a medial-lateral direction, whereas in the 2DOF cases, an additional rotational component was included, reproducing the characteristic convergent-divergent mucosal wavelike motion as displayed in Figure 3. Therefore, the medial surfaces of the vocal folds (red boundary in Figure 3) were considered to be rigid, and the translational and rotational motions were applied on that part. The inferior (left) and superior walls (right) of the vocal folds move freely according to the position of the medial surface with a floating boundary condition, so that the mesh vertices on these boundaries were not constrained. The anterior and posterior walls were also permitted to move in-plane because of the medial surface motion. To construct the ELL glottis constriction for the last case 2DOF + VeF-ELL, a sinusoidal function in the anterior-posterior direction was applied to the translational motion of the vocal folds, so that the time-dependent glottal area was the same as before. This function is

$$\Delta Y_{\text{ELL}} = \frac{\sin\left(2\pi\left(\frac{Z}{L} - \frac{1}{4}\right)\right) + 1}{2} \Delta Y, \quad (1)$$

where  $\Delta Y$  is the translational motion,  $Z$  is the anterior-posterior direction, and  $L$  is the length of vocal folds in the same direction.

**TABLE 2.**  
**Simulation Cases and Their Properties**

Case	Inlet	Glottal Duct Shape	Glottis Shape	Minimum Glottal Width
Static	Periodic flow rate	Convergent	Rectangular	1.5 mm
1DOF	Constant pressure	Convergent	Rectangular	0.2–2.3 mm
2DOF	Constant pressure	Convergent-divergent	Rectangular	0.2–2.3 mm
2DOF + VeF	Constant pressure	Convergent-divergent	Rectangular	0.2–2.3 mm
2DOF + VeF-ELL	Constant pressure	Convergent-divergent	Elliptical	0.2–4.6 mm

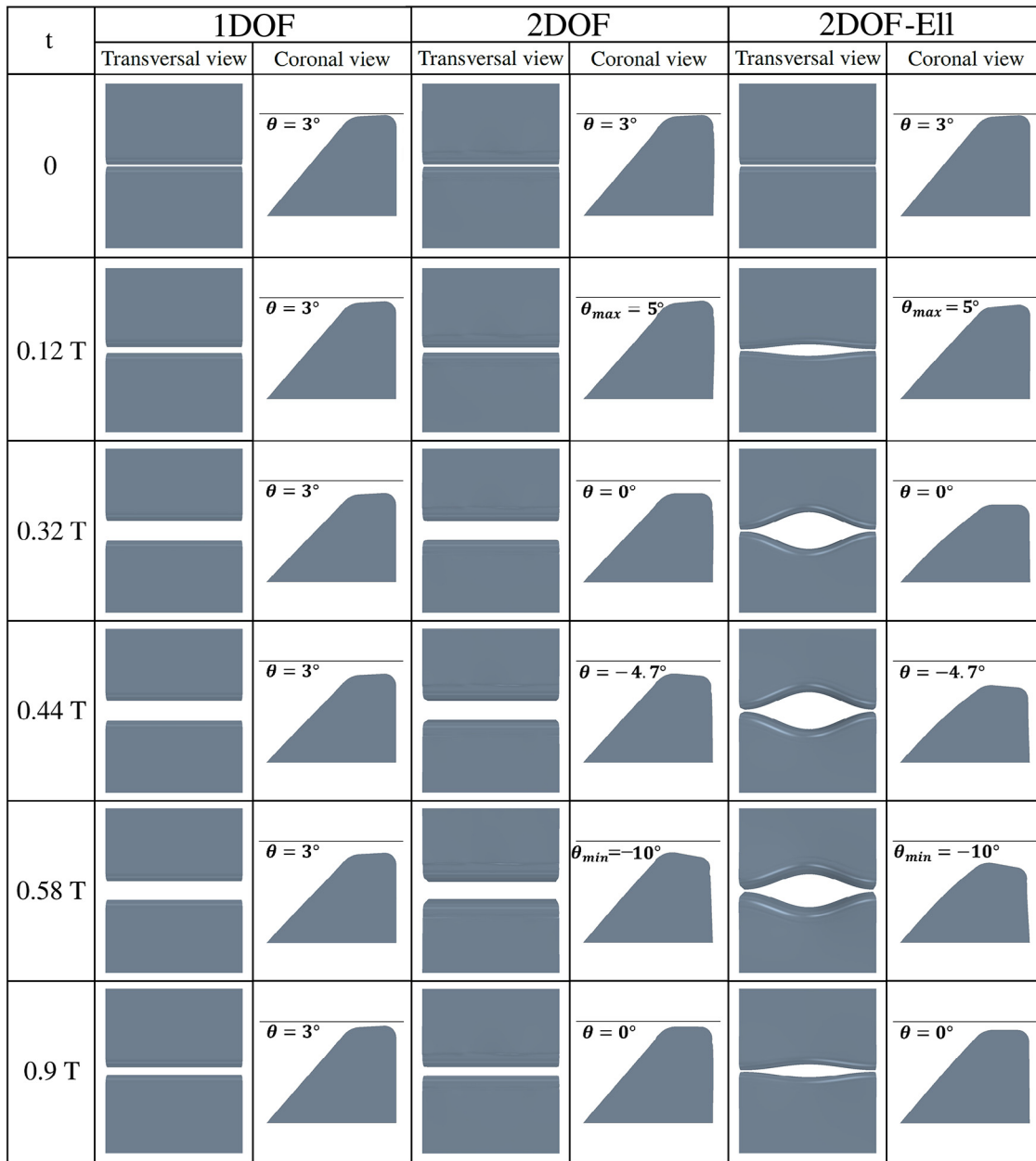


**FIGURE 4.** Oscillation pattern of the vocal fold dynamics for all simulation cases and their properties.

The frequency of the mass flow variation in the static case and the frequency of the vocal fold oscillation in the dynamic cases were selected as  $f_0 = 148$  Hz.

For the cases 2DOF + VeF and 2DOF + VeF-Ell, the VeFs were inserted. Because VeFs rarely vibrate in normal phonation,<sup>18,20</sup> they were designed on the basis of the static vocal fold geometry (M5 model) with a straight passage followed by a divergent expansion. The VeFs were positioned 7.5 mm downstream of the true vocal folds. The ventricular gap and the duct length were 5 and 10 mm, respectively.

The vocal fold dynamics from superior and coronal perspectives are given in Figure 4. The displayed instances are related to the beginning of the cycle ( $t = 0$ ), the maximum glottal convergent angle ( $t = 0.12T$ ), the straight glottis and the instance of changing to a divergent shape ( $t = 0.32T$ ), the maximum glottal

opening ( $t = 0.44T$ ), the maximum glottal divergent angle ( $t = 0.58T$ ), and the time to change again to a convergent shape ( $t = 0.9T$ ). These time points are also shown in Figure 2.

All cases with vocal fold motion have an open quotient of 0.93 and a speed quotient of 0.67 (physiological range:  $OQ = 0.4$ – $1.0$  and  $SQ = 0.6$ – $1.6$ <sup>58–61,80</sup>). In that context, the closed phase was defined when the glottal diameter reached its minimum of 0.2 mm.

### Boundary conditions

At the inlet boundary of the model, a periodic inlet mass flow as shown in Figure 5 was set for the static case with rigid vocal folds. The mass flow was approximated on the basis of the glottal jet velocity and the glottal area waveform, both obtained from experiments with the synthetic larynx model.<sup>77,87</sup> For the cases

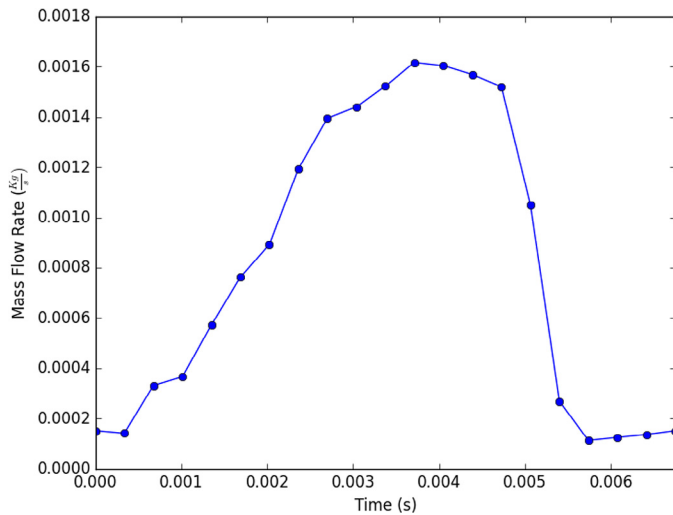


**FIGURE 5.** Periodic mass flow rate during one cycle of vocal fold oscillations obtained from the experiments.<sup>77,87</sup> The fundamental frequency of the vocal fold oscillation was  $f_0 = 148$  Hz.

with moving vocal folds, a constant pressure was set at the inlet that corresponds to the mean subglottal pressure obtained from the static simulation case. At the outlet boundary, the pressure was set to be constant at 0 kPa for all five simulation cases.

For the remaining boundary walls, no-slip and no-injection boundary conditions were imposed. The density and the kinematic viscosity of air were specified as  $\rho = 1.18415$  kg/m<sup>3</sup> and  $\nu = 1.5666 \times 10^{-5}$  m<sup>2</sup>/s, respectively. Owing to the Mach number being lower than 0.3 as found in experiments,<sup>1</sup> the density was assumed to be constant, resulting in an incompressible fluid flow.

### Numerical methods

The commercial software package *STAR-CCM+* (Siemens PLM software, Plano, TX/USA) was applied to simulate the fluid flow through the larynx model. A cell-centered nonstaggered FVM was used to solve the incompressible Navier-Stokes equations. The convective and diffusive terms of the Navier-Stokes equations were discretized using central difference schemes with second-order accuracy. For the pressure-velocity coupling, the PISO (Pressure-Implicit with Splitting of Operators) algorithm<sup>94</sup> was applied within a predictor-corrector scheme. The resulting linear system was solved iteratively by an algebraic multigrid method with a Gauss-Seidel relaxation scheme.

For turbulence modeling, large eddy simulation was performed with the WALE (wall-adapting local eddy-viscosity) subgrid-scale model<sup>95</sup> to resolve typical turbulent characteristics such as shear layer instabilities of the glottal jet as shown representatively in Figure 6. The near-wall flow was modeled by the *all* -  $y^+$  wall treatment provided by *STAR-CCM+*, which

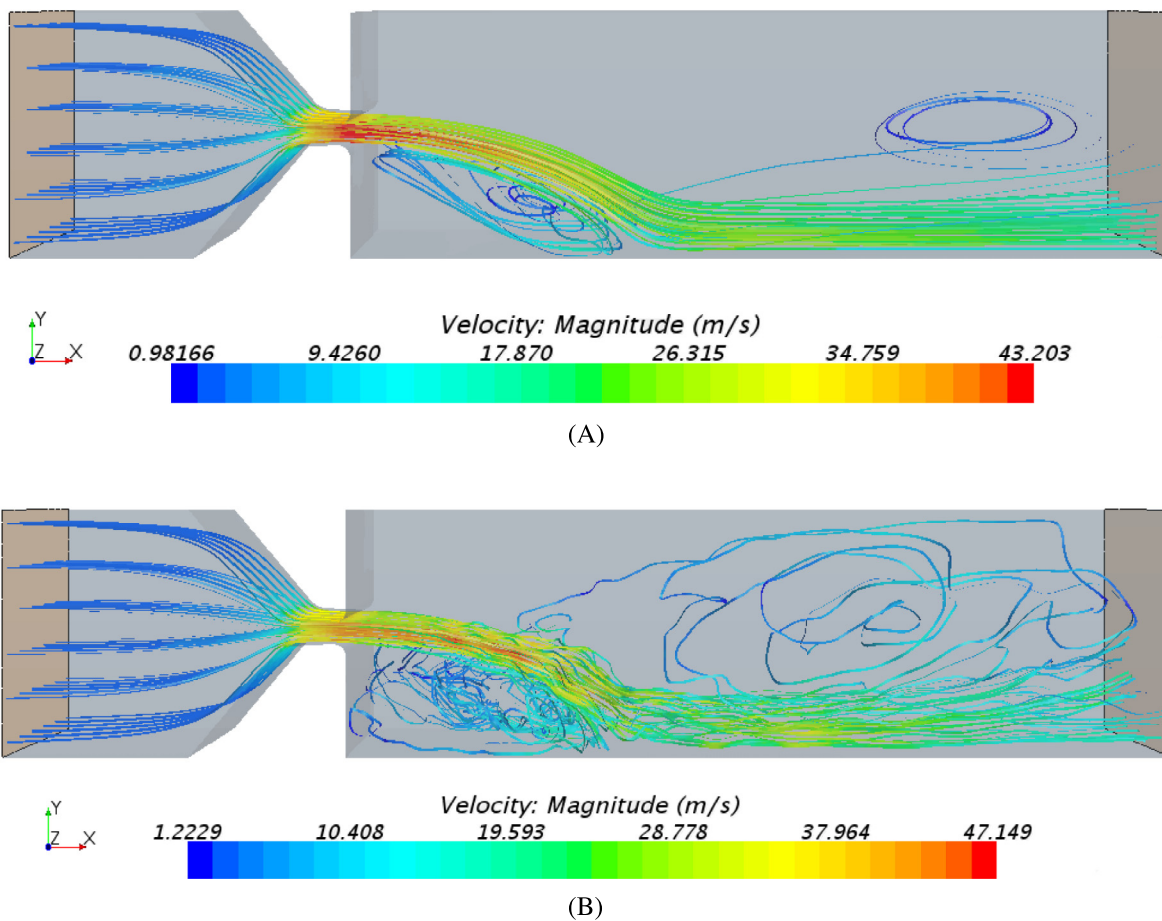


**FIGURE 6.** Stream line at  $t = 50$  ms for (A) SST (shear stress transport)  $k-\omega$  and (B) LES turbulence models.

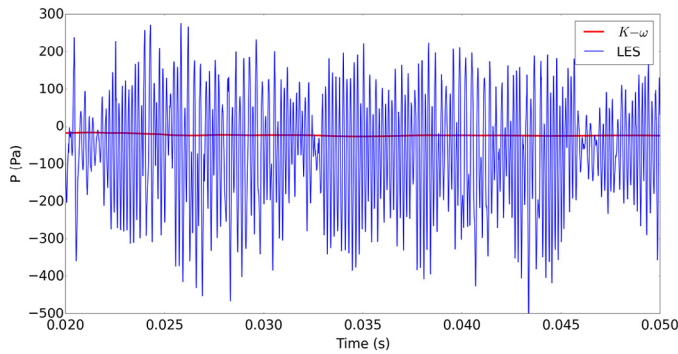


**FIGURE 7.** Temporal deviation of pressure 8 mm downstream in the supraglottal channel for SST (shear stress transport)  $k-\omega$  and LES calculations.

is a hybrid model of  $high - y^+$  and  $low - y^+$  wall treatments for coarse and fine meshes, respectively.

In comparison, much cheaper simulations on the basis of the unsteady Reynolds-averaged Navier-Stokes (URANS) equations for turbulence modeling reproduce the asymmetric glottal jet location as depicted in Figure 6A. However, the typical shear layer instabilities of the glottal jet are averaged out by the URANS methodology.

The reproduction of those instabilities is mandatory with regard to the correct determination of the acoustic sources. Common aeroacoustic analogies such as the Lighthill analogy<sup>96,97</sup> or the acoustic perturbed equation<sup>98</sup> are based on acoustic source formulations representing velocity and pressure fluctuations of the underlying fluid flow. These fluctuations of the flow variables are almost totally attenuated when using URANS, as illustrated in Figure 7.

### Numerical mesh motion approach

Critical problems with the numerical grid quality arise from large deformations of the mesh, especially during intervals of a small glottal gap within each oscillation cycle of the vocal folds. These problems limit the application of the numerically expensive ALE strategy for handling the numerical mesh deformation. In this approach, the total number of cells remains constant, but the cells were deformed according to the deformation of the boundary walls. Especially during phases with narrow glottal duct or contact between both vocal folds, extremely distorted cells with a zero

or even negative volume impair the numerical simulation and lead to a break-off in the worst case.

To overcome these problems, the overset mesh approach provided by *STAR-CCM+* was used in this work, which is based on the idea of fixed grid approaches in combination with overlapping domain decomposition and Chimera schemes.<sup>99</sup> In this method, a fixed Eulerian background mesh is assigned to the whole numerical domain (Figure 8A) and deformable overset meshes wrapped around both vocal folds (Figure 8B). Between the background and overset meshes, a small interface layer of cells indicated in blue in Figure 8 is included for interpolating the flow variables from the background to the overset mesh and vice versa. Wherever the overset and background meshes overlap, the occluded cells of the background mesh become inactive and the overset cells become active. At large glottis diameters, the overset mesh moves almost freely with only small deformations that occur owing to the stretching or compression of the vocal fold surface during their motion. At small glottis diameters, only the overset mesh exists in the glottal gap and is deformed according to the position and the shape of the vocal folds. With this approach, the ALE domain is closely limited to regions around the deformable walls of the vocal folds whereas the background mesh remains unchanged. To avoid elements with zero or even negative volume directly in the glottis, at least four cells remain between the vocal folds during glottis closure corresponding to a minimum glottal gap of 0.2 mm. This results in a small, negligible flow leakage. With regard to the numerical mesh size, the total number of cells is not constant during the simulation but depends on the distance between the vocal folds.

## RESULTS AND DISCUSSION

### Mesh independence study

The numerical mesh used in the present study is the result of a mesh independence study that analyzed the dependence of the flow field on the spatial resolution of the mesh and in the case of unsteady fluid flows on the temporal resolution (ie, the time step size). For the presented flow case of phonation, five different meshes were evaluated with their properties as shown in Table 3. The table includes the respective base size of the mesh and the target values for cell sizes after a refinement in the ROI (basic refinement), in the glottis region (glottis refinement), and

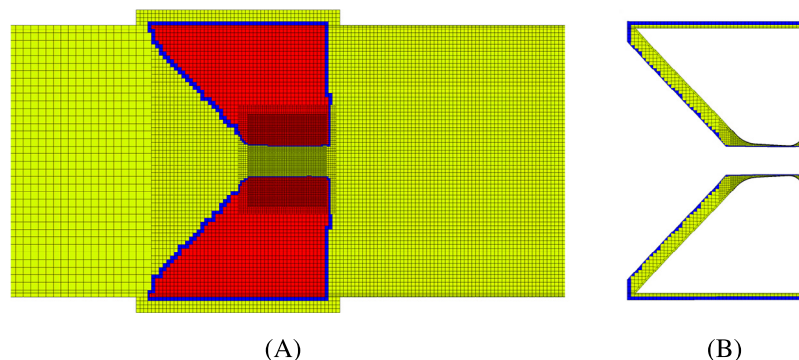


**FIGURE 8.** (A) Background and (B) overset meshes. Color legend: *red* for inactive cells, *yellow* for active cells, and *blue* for the cells at the interface. (For interpretation of the references to color in this figure legend, the reader is referred to the Web version of this article.)

**TABLE 3.**  
**Summary of Meshes Used for the Mesh Independence Study and Their Properties**

Mesh	Base Size (mm)	Basic Refinement (mm)	Glottis Refinement (mm)	Supraglottal Refinement (mm)	Total Number of Cells
M1	0.5	0.25	—	—	782,458
M2	0.5	0.25	0.125	—	862,565
M3	0.5	0.25	0.0625	—	1,464,075
M4	0.5	0.25	0.03125	—	6,222,014
M5	0.5	0.25	0.0625	0.125	2,274,647

Basic refinement applied to the base mesh refers to halving the mesh size in the glottal and near-supraglottal regions.

in the supraglottal region (supraglottal refinement). The ROI starts at the glottal inlet and ends up 36 mm downstream of the glottal exit. As result, the total number of cells of each mesh is displayed.

All meshes are assembled of hexahedral cells as displayed in Figure 9. The first mesh, M1, represents the starting mesh with the coarsest spatial resolution. It is structured in the inlet region, the outlet region, and the ROI. Whereas the numerical mesh in the inlet and outlet regions is coarse, the ROI has a higher resolution by halving the reference size of the mesh cells. For meshes M2–M4, the spatial resolution in the immediate glottal region between the vocal folds is systematically increased, as shown in Figure 9B–E. This results in an increase in the total number of cells, rising by a factor of approximately 8 from 782,458 to 6,222,014. In contrast, the mesh M5 represents a special case of M3 with an additional increase in resolution along the center line of the supraglottal channel to account for the glottal jet dynamics (Figure 9E).

To judge the quality of the proposed numerical meshes, an LES was performed for all five meshes with a constant pressure difference of 1 kPa and static vocal folds. The results were analyzed at discrete positions in the flow region. Figure 10 shows the time-averaged velocity profile at the minimum glottal area and 10 mm further downstream in the supraglottal region.

Within the glottis, the coarsest mesh M1 produces an over-estimated velocity magnitude profile with a visible asymmetric distribution along the glottal diameter. Further downstream at the point 10 mm, M1 produces an underestimated velocity magnitude with a high degree of asymmetry. By increasing the mesh resolution, the degree of asymmetry decreases (see Figure 10A) and the maximum velocity magnitude increases (see Figure 10B), converging to the mesh-independent flow field represented by M3 and M4. The same behavior can be seen for the static pressure distribution along the center line of the whole simulation

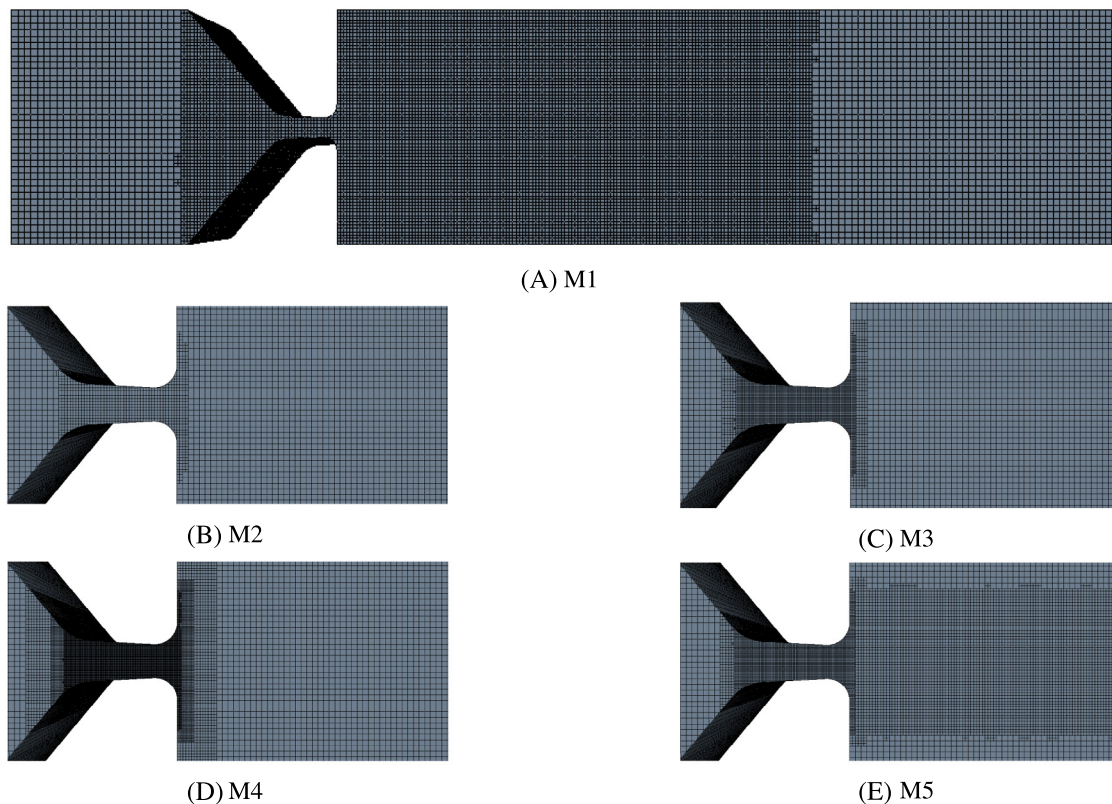


**FIGURE 9.** Numerical meshes (A–E) M1–M5 with different spatial resolutions for performing a mesh independence study.

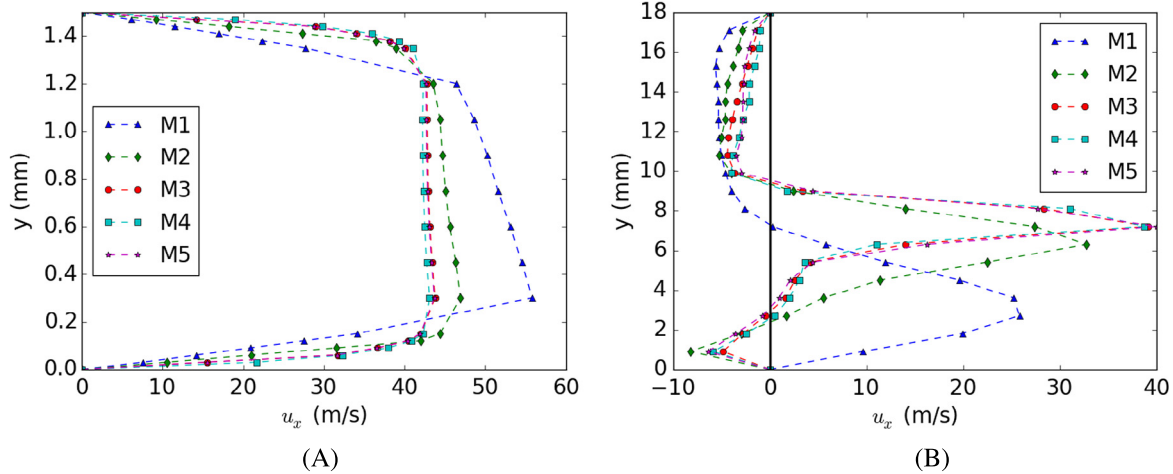


**FIGURE 10.** Time-averaged axial velocity profile in the midcoronal plane at (A) the minimum glottis area and (B) 10 mm upstream in the supraglottal region for different grids.

region as depicted in Figure 11. The additional refinement along the center line in the supraglottal region does not show a visible effect. Comparison of the time-averaged flow rates also showed an overestimation of 25% and 8% by the M1 and M2 meshes,

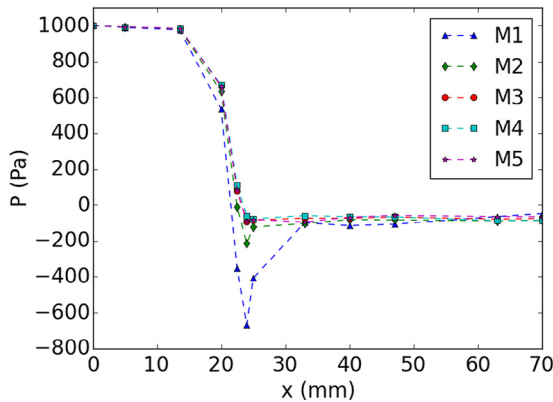


**FIGURE 11.** Time-averaged static pressure at some probes at the center line of the midcoronal plane for different grids.

respectively, but less than a 1% discrepancy for the other meshes with higher spatial resolutions.

In summary, meshes M3–M5 produce comparable results. Hence, the mesh M3 was chosen for the simulation because it exhibits the least control volumes.

As flow separation in the glottis is of great interest,<sup>100,101</sup> five additional prism layers are inserted along the glottal duct. In contrast to the basic mesh structure of M3 in the duct shown in Figure 12A, the prism layers produce a structure that exhibits layers parallel to the wall surface as displayed in Figure 12B. This parallelity is necessary to resolve properly the velocity gradient in the boundary layer with the aim of correctly simulating flow separation in the glottal duct. As a criterion for an appropriate orthogonal spacing of the prism layers, the nondimensional wall-normal coordinate  $y^+$  of the first cells is equal to 1, satisfying a common condition in numerical simulation of turbulent flows.<sup>102</sup>

Based on mesh M3, inserting the prism layers increases the number of elements in the numerical grid to 1,787,758, being still lower than that for M4 (Table 3). For the simulation cases

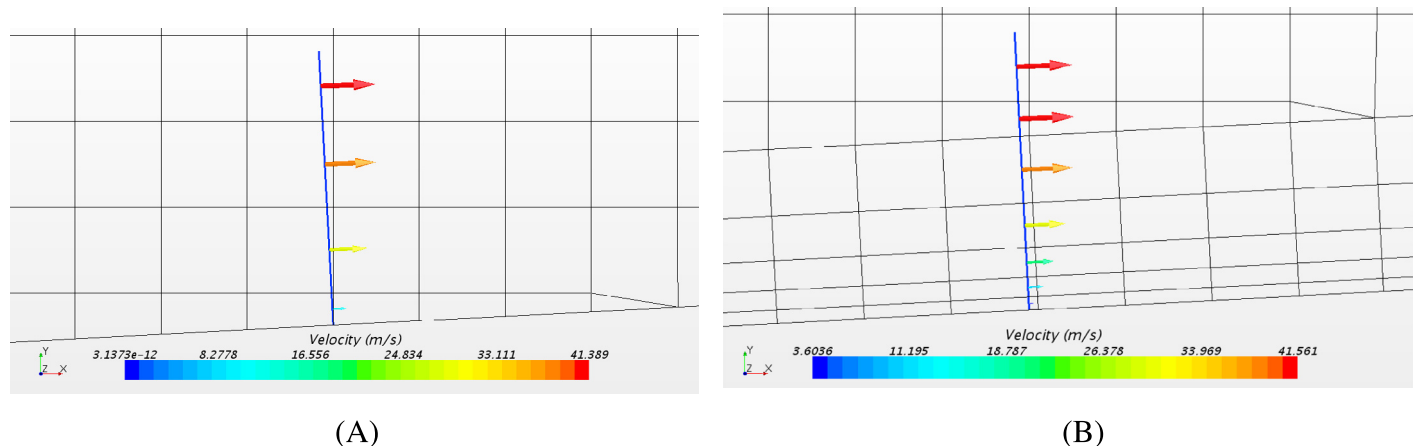


**FIGURE 12.** Grid resolution in the  $y$ - $x$  midplane and the boundary layer velocity vectors along an axis 1.5 mm upstream in the glottis: (A) without prism layer and (B) with five prism layers.

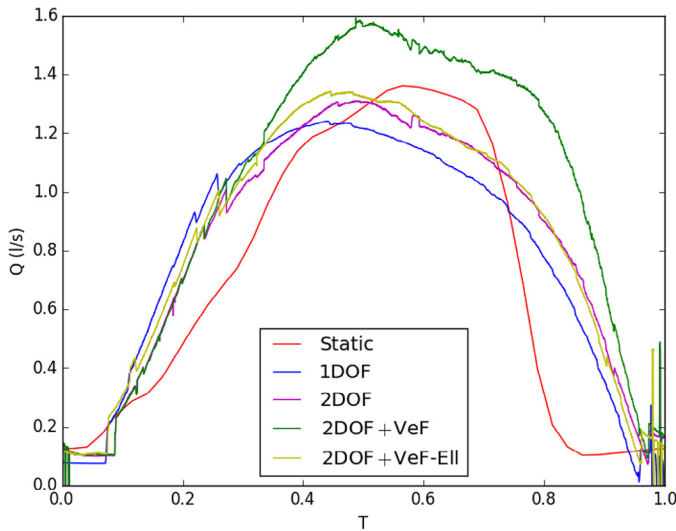


**FIGURE 13.** Flow rate for one oscillation cycle and all simulation cases.

with oscillating vocal folds, the mesh properties obtained from the mesh independence study were equally selected for generating the background and overset mesh.

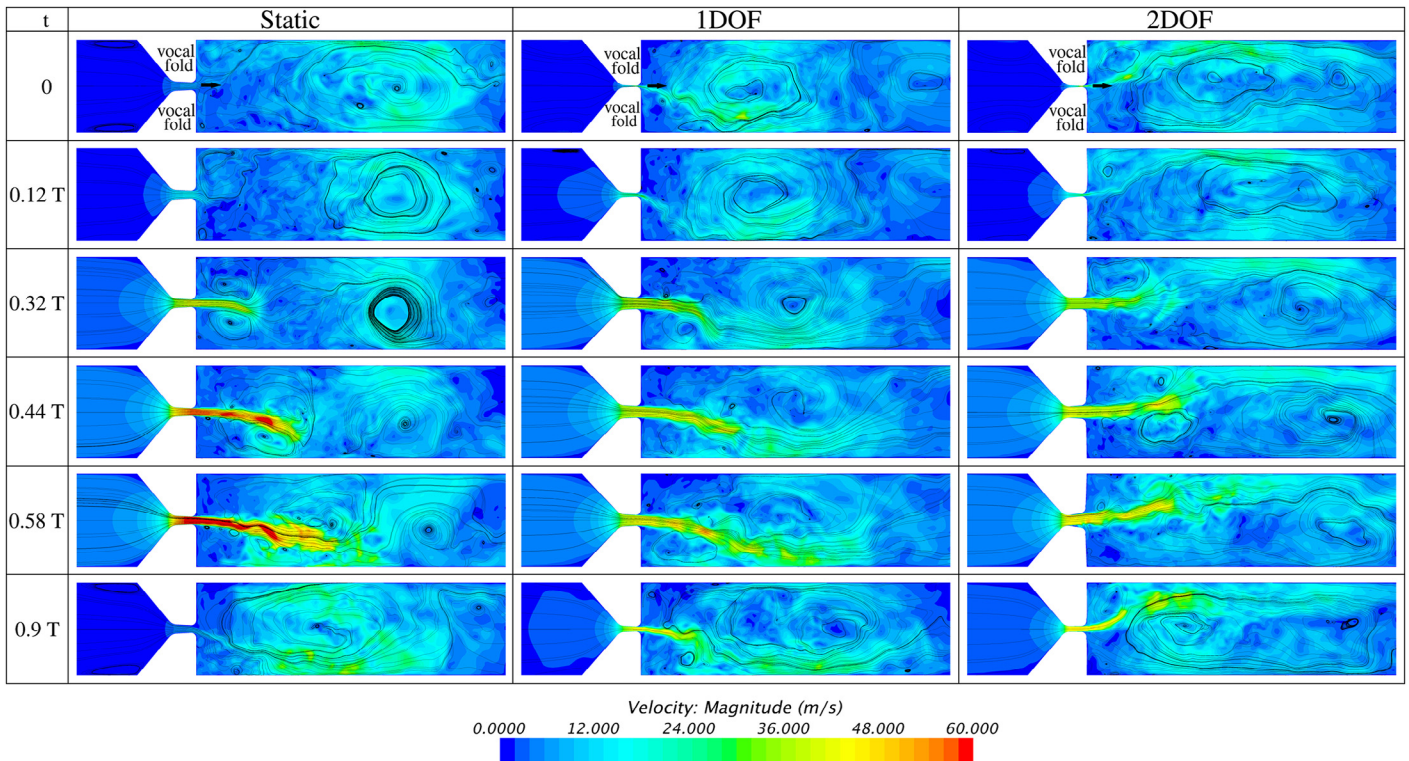
Finally, the time step size was selected as  $1 \times 10^{-6}$  s, which satisfies the Courant-Friedrichs-Lewy (*CFL*) condition  $CFL = 1$  in the ROI.<sup>103</sup> The *CFL* number describes the number of mesh cells that are transited by a fluid element during one time step.

**Glottal aerodynamics**

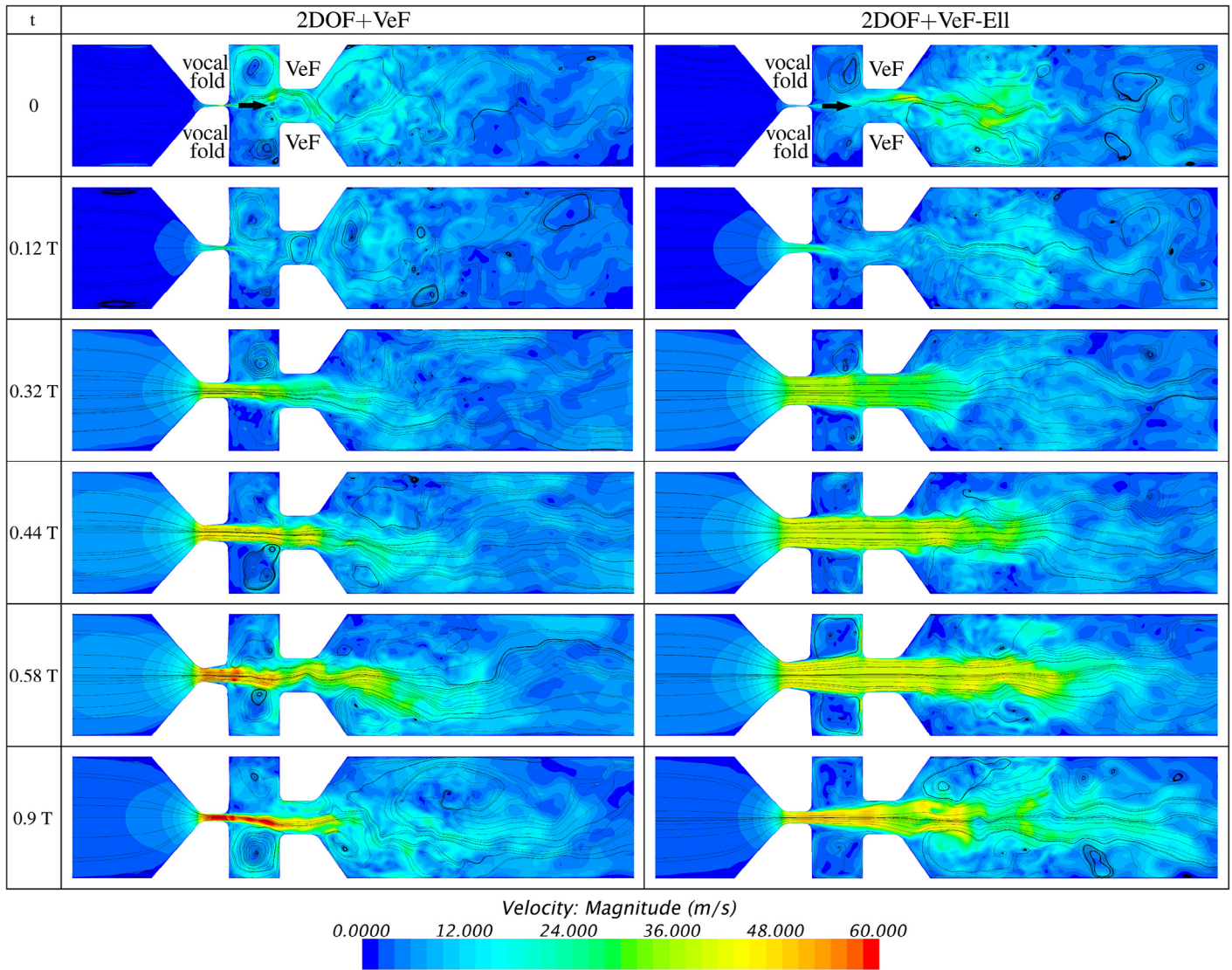
As described earlier, a varying flow rate according to the experiments was set as the inlet boundary condition to drive the flow through the static vocal folds (static case), which resulted in a mean pressure difference of  $\Delta P = 775$  Pa across the whole numerical domain, which is in the typical range during human phonation.<sup>79</sup> For the other cases with driven vocal fold motion, the flow was generated by a mean pressure difference between inlet and outlet also equal to  $\Delta P = 775$  Pa.

Figure 13 shows the flow rate through the larynx model for one oscillation cycle for all cases. The peak flow rate increases with increasing degree of realism from the 1DOF to the 2DOF + VeF case. Therein, the increase between 1DOF and 2DOF is mainly attributed to the divergent glottal duct shape that operates as a diffuser decreasing the flow resistance of the glottal constriction.<sup>23,24,43</sup> Furthermore, the peak is delayed in the oscillation cycle compared with 1DOF owing to the occurrence of the divergent duct shape in the second half of an oscillation cycle. The further increase in mass flow in the 2DOF + VeF case is caused by the presence of the VeFs. This was similarly reported by Zheng et al,<sup>69</sup> who also found an increase in mass flow caused by a decrease in laryngeal resistance in the presence of the VeFs.

By further involving the ELL glottis shape, the peak flow rate declines compared with the rectangular glottis. By maintaining the same glottal area function of rectangular glottis shape in 2DOF + VeF, the maximum glottal diameter is increased. Furthermore, an increasing transversal expansion of the glottal jet downstream of the vocal folds could be observed, which origi-



**FIGURE 14.** Velocity magnitude with streamlines in the midcoronal plane of the static, 1DOF, and 2DOF cases at six instances of the 10th cycle. The six instances of the cycle correspond to those shown in Figure 2. The arrows show the flow direction.



**FIGURE 15.** Velocity magnitude with streamlines in the midcoronal plane for the 2DOF + VeF and 2DOF + VeF-Ell cases at six instances of the 10th cycle. The six instances of the cycle correspond to those shown in Figure 2. The arrows show the flow direction.

nated from the axis-switching process that was attributed to the ELL glottis shape by Triep and Brücker.<sup>104</sup> By this expansion, the interaction of the glottal jet with the VeFs is increased, as shown in Figure 15 for the 2DOF + VeF-Ell case, which may result in flow rate decay.

The supraglottal flow field for all simulation cases without VeFs is depicted in Figure 14 at six instances during an oscillation cycle related to Figure 4. Accordingly, the flow fields for the cases with VeFs are depicted in Figure 15. All cases except those including VeFs show the typical glottal jet deflection that has often been described in experimental<sup>105–108</sup> and numerical larynx models.<sup>24,31</sup> The jet deflection is caused by the interaction of the glottal jet with large vortex structures in the supraglottal region.<sup>31,77,87</sup> Thereby, the direction of jet deflection is determined by the rotation direction of the large vortex that extends across the whole height of the channel as indicated in Figure 14. A clockwise rotating vortex forces the jet to deflect in the upward direction as shown for the 2DOF case and a counterclockwise

rotating vortex causes a deflection in the downward direction shown for the 1DOF and static cases. The maximum angle between the jet and the center axis of the supraglottal channel is larger for cases with moving vocal folds (1DOF and 2DOF) owing to smaller absolute velocities in the jet core. The direction and the angle of deflection could also change from cycle to cycle depending on the position and the direction of the recirculation area. This change of deflection direction happens less frequently by increasing the degree of realism of the model, so that for the 2DOF case, it did not occur during 10 cycles (see Supplementary Videos S1–S3). This behavior was also reported by Lou *et al.*<sup>45</sup> In addition to the interaction of the jet with the large recirculation area, shear layer instabilities occur that additionally deviate the tail of the jet. By including the VeFs, the jet deflection is drastically reduced. As consequence, the glottal jet is straightened and elongated compared with cases without VeFs, as depicted in Figure 15. The same phenomenon was also observed in numerical larynx models.<sup>69,109</sup>

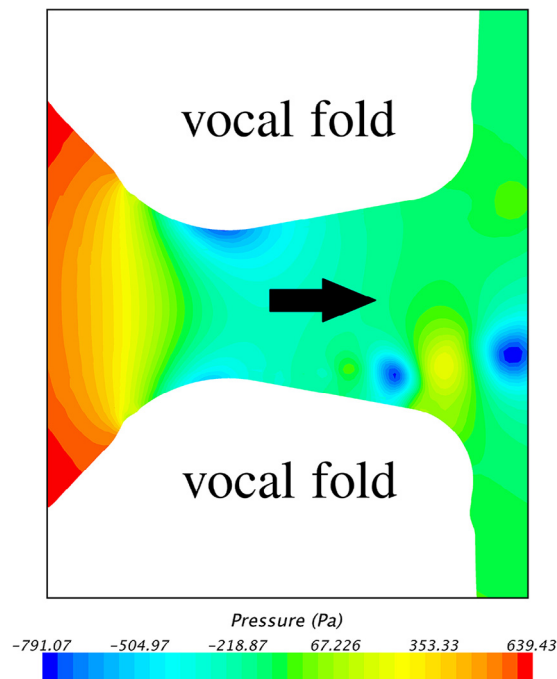


**FIGURE 16.** Intraglottal pressure distribution of the case 2DOF at the time point 0.58 T. The intraglottal vortices can be seen as the areas with drastically lower pressures relative to their surroundings. The arrow shows the flow direction.

Regarding the flow within the glottal duct, the glottal jet remains almost completely attached to both vocal folds in the static and 1DOF cases. In contrast, by introducing the mucosal wave motion in the 2DOF cases, the jet separates from one vocal fold and reattaches to the other during the closing motion. This flow separation occurs within the divergently shaped glottal duct. The resulting small vortices are shown in Figure 16 for the case 2DOF and were similarly found by Khosla et al and Oren et al<sup>100,101</sup> in excised larynx studies.

By introducing the ELL glottis shape, the jet flow becomes totally 3D in the sagittal plane represented by a decreasing jet diameter in the longitudinal direction of the glottis, as shown in Figure 17. This was similarly reported by Triep and Brücker,<sup>104</sup> who used a synthetic, experimental larynx model operating with water. The constriction of the glottal jet in the sagittal plane was due to the axis-switching process of the glottal jet induced by the ELL glottis shape. This three dimensionality of the glottal jet was also confirmed in computational larynx models.<sup>29,33,64</sup>

### Computational cost

The simulations in the present study were performed on five computer nodes of RRZE's Emmy cluster of the University of Erlangen-Nürnberg,<sup>110</sup> with 20 Intel Xeon 2660v2 cores each (25M Cache, 2.2 GHz, 40 threads per node owing to hyperthreading). Therefore, the simulation is decomposed into 200 threads, with each two of these threads allocated to one physical processor for execution. Table 4 summarizes the mesh size and the computational cost of each simulation case for 10 oscillation cycles, resulting in 67,500 time steps.

**TABLE 4.** Mesh Resolution and Computational Cost for 10 Cycles of Simulation

Case	Resolution (Cells)	Total CPU Time (h)	Wall Time (h)
Static	1.78M	4,970	25
1DOF	1.68–2.39M	42,180	212
2DOF	1.68–2.37M	56,156	282
2DOF + VeF	1.58–2.24M	57,152	289
2DOF + VeF-Ell	1.57–2.25M	55,919	281

The elapsed simulation time increased with the complexity of the modeling and the flow field. The elapsed simulation time increased by a factor of approximately 11 from the static case to the convergent-divergent motion of vocal folds, although the average number of cells had a growth of only 20%. There are several reasons that account for this increase:

- The mesh has to be updated in each time step for dynamic cases. In particular, updating the interfaces between the oversets and background meshes increases the computational time severely in each time step.
- An increase in complexity of the flow field affects both the convergence rate and the complexity of the coarser level matrices in the algebraic multigrid solver, which increases both run-time and memory requirements. Intraglottal flow separation, glottal jet interaction with VeFs, and 3D development of glottal jet are examples of such complexities.
- Recalculation of the wall distance within the boundary layer flow model for LES in each time step due to the movements of the boundary nodes also increases the calculation time.

The results show that for an effective application of computational larynx models in clinical environments, the computational effort is too large. However, in voice research, especially for the investigation of voice pathologies, these models have great potential in developing new therapy strategies.

### SUMMARY AND CONCLUSION

The 3D laryngeal airflow was numerically simulated with the commercial FVM solver *STAR-CCM+* for different models of vocal fold dynamics. In addition to a simulation case with static vocal folds and oscillating inlet flow rate condition, the vocal fold motion was externally driven by prescribing the motion of glottal walls that shaped the vocal folds. Thus, for all cases, a pure simulation of the fluid dynamics was performed. The size and the structure of the numerical mesh for all cases were determined by a mesh independence study. To evaluate the numerical effort, the vocal fold motion was modeled with increasing degree of realism; that is, single characteristic features of the physiological phonation process were added in different simulation cases: (1) static vocal folds, (2) transversal oscillation of vocal folds, (3) mucosal wave motion of vocal folds, (4) inclusion of VeFs

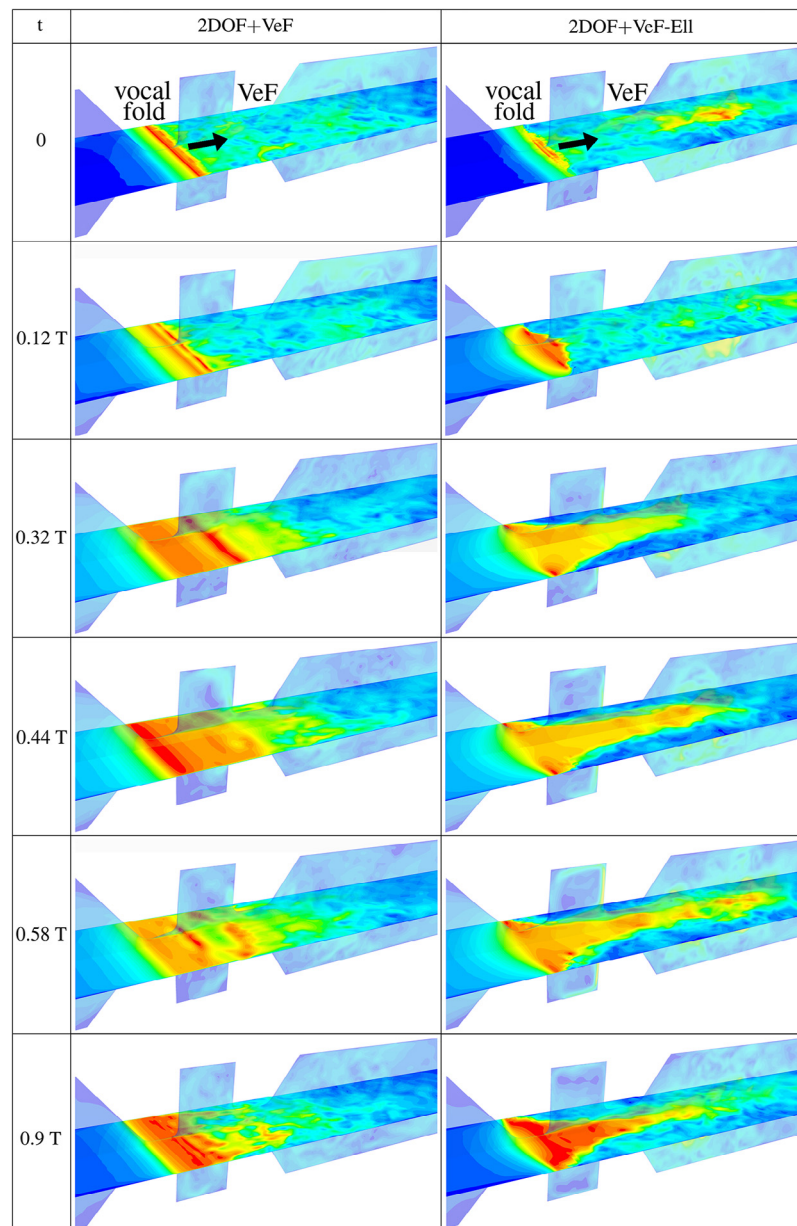


**FIGURE 17.** Velocity contours in the midsagittal plane of the 2DOF + VeF and 2DOF + VeF-ELL cases at the six instances of the cycle. The arrows show the flow direction.

(all with rectangular glottis shape), and finally, (5) with the ELL glottis shape. The geometric and dynamic data for the different models were taken from experimental data obtained from a synthetic larynx model with synthetic vocal folds made of silicone being based on the M5 model.

The numerical meshes contain between 1.58 and 2.39 million cells depending on the glottis diameter and the particular simulation case. LES was performed for each case to simulate 10 oscillation cycles. Even though none of the numerical models included the direct fluid-structure interaction that is characteristic for the phonation process, the resulting flow fields reproduced characteristic features of the laryngeal airflow as reported in the literature. Whereas glottal jet deflection was found for all cases without VeFs, intraglottal flow separation was most distinct for the case with mucosal wave motion. The inclusion of the VeFs

resulted in an increase in flow rate owing to the decrease in laryngeal flow resistance. By introducing an ELL glottis shape, the glottal jet became 3D, showing a constriction in the sagittal plane and a slight increase in the midcoronal plane similar to the axis-switching mechanism found in experiments.

The numerical effort was measured by the CPU time as the time for one physical core summed over all cores. Each simulation was computed on the compute cluster of the University of Erlangen using 100 physical cores. The CPU time increased drastically with increasing degree of realism. The associated wall time (CPU time divided by the number of cores plus communication processes) of a simulation ranges between 25 hours for static vocal folds and 281 hours for forced motion with a mucosal wave, ELL glottis shape, and VeFs. This increase by a factor of more than 11 is attributed to several reasons, such as the adaption

of the numerical mesh during the oscillation to maintain suitable mesh conditions. Other reasons are the increase in complex flow structures such as the supraglottal vortex field and the interaction of the glottal jet with the VEFs, resulting in large velocity gradients.

Owing to the large wall time and the highly parallel compute cluster needed, such numerical models are hardly able to fulfill the requirements of daily clinical application. However, numerical models are very important in research. Only by a hybrid strategy of equal usage of experimental and numerical models will the complex process of fluid-structure-acoustic interactions be completely understood. Finally, numerical models in daily clinical use are highly important and the development of such clinical models should be continued.

### Acknowledgments

The authors acknowledge support from the German Research Foundation (DFG) under DO1247/10-1 no. 391215328, the Austrian Research Council (FWF) under no. I 3702, and the Central Institute for Scientific Computing (ZISC), and the computational resources and support provided by the Erlangen Regional Computing Center (RRZE).

### SUPPLEMENTARY DATA

Supplementary data related to this article can be found online at doi:10.1016/j.jvoice.2018.01.001.

### REFERENCES

- Kniesburges S, Thomson S, Barney A, et al. In vitro experimental investigation of voice production. *Curr Bioinform.* 2011;6:305–322. doi:10.2174/157489311796904637.
- Mittal R, Zheng X, Bhardwaj R, et al. Toward a simulation-based tool for the treatment of vocal fold paralysis. *Front Physiol.* 2011;2:doi:10.3389/fphys.2011.00019.
- Liljencrants J. Numerical simulations of glottal flow. *STL-QPSR.* 1989;30:69–74.
- Iijima H, Miki N, Nagai N. Glottal impedance based on a finite element analysis of two-dimensional unsteady viscous flow in a static glottis. *IEEE Trans Signal Process.* 1992;40:2125–2135. doi:10.1109/78.157213.
- Guo CG, Scherer RC. Finite element simulation of glottal flow and pressure. *J Acoust Soc Am.* 1993;94(2 pt 1):688–700. doi:10.1121/1.406886.
- Alipour F, Scherer RC, Knowles J. Velocity distributions in glottal models. *J Voice.* 1996;10:50–58. doi:10.1016/S0892-1997(96)80018-X.
- Scherer RC, Witt KJD, Kucinschi BR. The effect of exit radii on intraglottal pressure distributions in the convergent glottis. *J Acoust Soc Am.* 2001;110(5 pt 1):2267–2269. doi:10.1121/1.1408255.
- Li S, Scherer RC, Wan M, et al. The effect of entrance radii on intraglottal pressure distributions in the divergent glottis. *J Acoust Soc Am.* 2012;131:1371–1377. doi:10.1121/1.3675948.
- Li S, Scherer RC, Wan M, et al. The effect of glottal angle on intraglottal pressure. *J Acoust Soc Am.* 2006;119:539–548. doi:10.1121/1.2133491.
- Li S, Scherer RC, Wan M, et al. Numerical study of the effects of inferior and superior vocal fold surface angles on vocal fold pressure distributions. *J Acoust Soc Am.* 2006;119:3003–3010. doi:10.1121/1.2186548.
- Céré S, Lormand A, Redekop D, et al. Simulation of the three-dimensional flow in the human larynx. *Can Acoust.* 2007;35:116–117.
- Suh J, Frankel SH. Comparing turbulence models for flow through a rigid glottal model. *J Acoust Soc Am.* 2008;123:1237–1240. doi:10.1121/1.2836783.
- Mihaescu M, Khosla SM, Murugappan S, et al. Unsteady laryngeal airflow simulations of the intra-glottal vortical structures. *J Acoust Soc Am.* 2010;127:435–444. doi:10.1121/1.3271276.
- Scherer RC, Torkaman S, Afjeh AA. Intraglottal pressures in a three-dimensional model with a non-rectangular glottal shape. *J Acoust Soc Am.* 2010;128:828–838. doi:10.1121/1.3455838.
- Klostermann J, Schwarze R, Triep M, et al. Numerical simulations of three dimensional glottis flows. *PAMM.* 2008;8:10619–10620. doi:10.1002/pamm.200810619.
- Schwarze R, Mattheus W, Klostermann J, et al. Starting jet flows in a three-dimensional channel with larynx-shaped constriction. *Comput Fluids.* 2011;48:68–83. doi:10.1016/j.compfluid.2011.03.016.
- Li S, Wan M, Wang S. *The Effects of the False Vocal Fold Gaps in a Model of the Larynx on Pressures Distributions and Flows*, Vol. 4561. Berlin, Heidelberg: Springer; 2007:147–156. doi:10.1007/978-3-540-73321-8\_18.
- Chisari NE, Artana G, Sciamarella D. Experimental and numerical study of patterns in laryngeal flow. *J Phys Conf Ser.* 2009;166:012013.
- Chisari NE, Artana G, Sciamarella D. Vortex dipolar structures in a rigid model of the larynx at flow onset. *Exp Fluids.* 2010;50:397–406. doi:10.1007/s00348-010-0941-x.
- Farahani MH, Mousel J, Alipour F, et al. A numerical and experimental investigation of the effect of false vocal fold geometry on glottal flow. *J Biomech Eng.* 2013;135:1210061–12100611. doi:10.1115/1.4025324.
- Mihaescu M, Khosla SM, Ephraim GJ. Quantification of the false vocal-folds effects on the intra-glottal pressures using large eddy simulation. *Proc Meet Acoust.* 2013;19:doi:10.1121/1.4799796.
- Luzan CF, Chen J, Mihaescu M, et al. Computational study of false vocal folds effects on unsteady airflows through static models of the human larynx. *J Biomech.* 2015;48:1248–1257. doi:10.1016/j.jbiomech.2015.03.010.
- Zhao W, Frankel SH, Mongeau L. Numerical simulations of sound from confined pulsating axisymmetric jets. *AIAA J.* 2001;39:1868–1874. doi:10.2514/2.1201.
- Suh J, Frankel SH. Numerical simulation of turbulence transition and sound radiation for flow through a rigid glottal model. *J Acoust Soc Am.* 2007;121:3728–3739. doi:10.1121/1.2723646.
- Mihaescu M, Gutmark E, Khosla S, et al. Flow and Acoustics Simulations Based on LES and an Acoustic Analogy: An Application to Laryngeal Airflow. 45th AIAA Aerospace Sciences Meeting and Exhibit. 2007. doi:10.2514/6.2007-919.
- Alipour F, Fan C, Scherer RC. A numerical simulation of laryngeal flow in a forced-oscillation glottal model. *Comput Speech Lang.* 1996;10:75–93. doi:10.1006/csla.1996.0005.
- Sciamarella D, Quéré PL. Solving for unsteady airflow in a glottal model with immersed moving boundaries. *Eur J Mech B Fluids.* 2008;27:42–53. doi:10.1016/j.euromechflu.2007.06.004.
- Kucinschi BR, Scherer RC, DeWitt KJ, et al. An experimental analysis of the pressures and flows within a driven mechanical model of phonation. *J Acoust Soc Am.* 2006;119(5 pt 1):3011–3021. doi:10.1121/1.2186429.
- Mattheus W, Brücker C. Asymmetric glottal jet deflection: differences of two- and three-dimensional models. *J Acoust Soc Am.* 2011;130:EL373–EL379. doi:10.1121/1.3655893.
- Zörner S, Kaltenbacher M, Döllinger M. Investigation of prescribed movement in fluid-structure interaction simulation for the human phonation process. *Comput Fluids.* 2013;86:133–140. doi:10.1016/j.compfluid.2013.06.031.
- Zheng X, Mittal R, Bielamowicz S. A computational study of asymmetric glottal jet deflection during phonation. *J Acoust Soc Am.* 2011;129:2133–2143. doi:10.1121/1.3544490.
- Šimánek P, Feistauer M. Numerical simulation of compressible flow in an asymmetric vocal jet. *Proc World Congr Eng Comput Sci.* 2013; 2.
- Brücker C, Triep M, Mattheus W. Flow behaviour of the glottal jet in 2D-versus 3D-CFD modelling. Conference: AIA-DAGA Conference on Acoustics.
- Alipour F, Scherer RC. Flow separation in a computational oscillating vocal fold model. *J Acoust Soc Am.* 2004;116:1710–1719. doi:10.1121/1.1779274.

35. Kaltenbacher M, Zörner S, Hüppe A, et al. 3D numerical simulations of human phonation. 11th World Congress on Computational Mechanics (WCCM XI).
36. Šidlof P, Horáček J, Řídký V. Parallel CFD simulation of flow in a 3D model of vibrating human vocal folds. *Comput Fluids*. 2013;80:290–300. doi:10.1016/j.compfluid.2012.02.005.
37. Zörner S, Šidlof P, Hüppe A, et al. Flow and acoustic effects in the larynx for varying geometries. *Acta Acust United Acust*. 2016;102:257–267. doi:10.3813/AAA.918942.
38. Šidlof P, Zörner S, Hüppe A. Numerical simulation of flow-induced sound in human voice production. *Procedia Eng*. 2013;61:333–340. doi:10.1016/j.proeng.2013.08.024.
39. Šidlof P, Zörner S. Computational aeroacoustics of human phonation. *EPJ Web Conf*. 2013;45:010851.
40. Zörner S, Šidlof P, Hüppe A, et al. Acoustic perturbation equations and Lighthill's acoustic analogy for the human phonation. *J Acoust Soc Am*. 2013;133:3618. doi:10.1121/1.4806760.
41. Šidlof P, Zörner S, Hüppe A. A hybrid approach to the computational aeroacoustics of human voice production. *Biomech Model Mechanobiol*. 2015;14:473–488. doi:10.1007/s10237-014-0617-1.
42. Zhang C, Zhao W, Frankel S, et al. Computational aeroacoustics of phonation, part II: effects of flow parameters and ventricular folds. *J Acoust Soc Am*. 2002;112(5 pt 1):2147–2154. doi:10.1121/1.1506694.
43. Zhao W, Zhang C, Frankel S, et al. Computational aeroacoustics of phonation, part I: computational methods and sound generation mechanisms. *J Acoust Soc Am*. 2002;112(5 pt 1):2134–2146. doi:10.1121/1.1506693.
44. Bae Y, Moon YJ. Computation of phonation aeroacoustics by an INS/PCE splitting method. *Comput Fluids*. 2008;37:1332–1343. doi:10.1016/j.compfluid.2007.12.002.
45. Luo H, Mittal R, Zheng X, et al. An immersed-boundary method for flow-structure interaction in biological systems with application to phonation. *J Comput Phys*. 2008;227:9303–9332. doi:10.1016/j.jcp.2008.05.001.
46. Luo H, Mittal R, Bielamowicz SA. Analysis of flow-structure interaction in the larynx during phonation using an immersed-boundary method. *J Acoust Soc Am*. 2009;126:816–824. doi:10.1121/1.3158942.
47. Link G, Kaltenbacher M, Breuer M, et al. A 2D finite-element scheme for fluid-solid-acoustic interactions and its application to human phonation. *Comput Methods Appl Mech Eng*. 2009;198:3321–3334. doi:10.1016/j.cma.2009.06.009.
48. Kaltenbacher M, Zörner S, Hüppe A. On the importance of strong fluid-solid coupling with application to human phonation. *Prog Comput Fluid Dynam Int J*. 2014;14:2–13. doi:10.1504/PCFD.2014.059195.
49. Rosa MO, Pereira JC, Grellet M, et al. A contribution to simulating a three-dimensional larynx model using the finite element method. *J Acoust Soc Am*. 2003;114:2893–2905. doi:10.1121/1.1619981.
50. Xue Q, Zheng X, Mittal R, et al. Subject-specific computational modeling of human phonation. *J Acoust Soc Am*. 2014;135:1445–1456. doi:10.1121/1.4864479.
51. Tao C, Jiang JJ. A self-oscillating biophysical computer model of the elongated vocal fold. *Comput Biol Med*. 2008;38:1211–1217. doi:10.1016/j.combiomed.2008.10.001.
52. Jo Y, Ra H, Moon Y, et al. Three-dimensional computation of flow and sound for human hemilarynx. *Comput Fluids*. 2016;134–135:41–50. doi:10.1016/j.compfluid.2016.04.029.
53. Xue Q, Mittal R, Zheng X, et al. Computational modeling of phonatory dynamics in a tubular three-dimensional model of the human larynx. *J Acoust Soc Am*. 2012;132:1602–1613. doi:10.1121/1.4740485.
54. Xue Q, Zheng X, Mittal R, et al. Computational study of effects of tension imbalance on phonation in a three-dimensional tubular larynx model. *J Voice*. 2014;28:411–419. doi:10.1016/j.jvoice.2013.12.016.
55. Smith SL, Thomson SL. Influence of subglottic stenosis on the flow-induced vibration of a computational vocal fold model. *J Fluids Struct*. 2013;38:77–91. doi:10.1016/j.jfluidstructs.2012.11.010.
56. Duncan C, Zhai G, Scherer RC. Modeling coupled aerodynamics and vocal fold dynamics using immersed boundary methods. *J Acoust Soc Am*. 2006;120:2859–2871. doi:10.1121/1.2354069.
57. Alipour F. Pressure and velocity in a model of laryngeal ventricle, 8th International Workshop of Models and Analysis of Vocal Emissions for Biomedical Applications.
58. Thomson SL, Mongeau L, Frankel SH. Aerodynamic transfer of energy to the vocal folds. *J Acoust Soc Am*. 2005;118(3 pt 1):1689–1700. doi:10.1121/1.2000787.
59. Pickup BA, Thomson SL. Identification of geometric parameters influencing the flow-induced vibration of a two-layer self-oscillating computational vocal fold model. *J Acoust Soc Am*. 2011;129:2121–2132. doi:10.1121/1.3557046.
60. Smith SL, Thomson SL. Effect of inferior surface angle on the self-oscillation of a computational vocal fold model. *J Acoust Soc Am*. 2012;131:4062–4075. doi:10.1121/1.3695403.
61. Shurtz TE, Thomson SL. Influence of numerical model decisions on the flow-induced vibration of a computational vocal fold model. *Comput Struct*. 2013;122:44–54. doi:10.1016/j.compstruc.2012.10.015.
62. Xue Q, Mittal R, Zheng X, et al. A computational study of the effect of vocal-fold asymmetry on phonation. *J Acoust Soc Am*. 2010;128:818–827. doi:10.1121/1.3458839.
63. Zheng X, Xue Q, Mittal R, et al. A coupled sharp-interface immersed boundary-finite-element method for flow-structure interaction with application to human phonation. *ASME J Biomech Eng*. 2010;132:1110031–11100312. doi:10.1115/1.4002587.
64. Zheng X, Mittal R, Xue Q, et al. Direct-numerical simulation of the glottal jet and vocal-fold dynamics in a three-dimensional laryngeal model. *J Acoust Soc Am*. 2011;130:404–415. doi:10.1121/1.3592216.
65. Alipour F, Titze I. Combined simulation of two-dimensional airflow and vocal-fold vibration. *J Acoust Soc Am*. 1997;102:3204. doi:10.1121/1.420935.
66. Alipour F, Scherer RC. Vocal fold bulging effects on phonation using a biophysical computer model. *J Voice*. 2000;14:470–483. doi:10.1016/S0892-1997(00)80004-1.
67. Alipour F, Scherer RC. Time-dependent pressure and flow behavior of a self-oscillating laryngeal model with ventricular folds. *J Voice*. 2015;29:649–659. doi:10.1016/j.jvoice.2014.10.021.
68. Vries MP, Schutte HK, Veldman AEP, et al. Glottal flow through a two-mass model: comparison of Navier-Stokes solutions with simplified models. *J Acoust Soc Am*. 2002;111:1847–1853. doi:10.1121/1.1323716.
69. Zheng X, Bielamowicz SA, Luo H, et al. A computational study of the effect of false vocal folds on glottal flow and vocal fold vibration during phonation. *Ann Biomed Eng*. 2009;37:625–642. doi:10.1007/s10439-008-9630-9.
70. Tao C, Jiang JJ, Zhang Y. Simulation of vocal fold impact pressures with a self-oscillating finite-element model. *J Acoust Soc Am*. 2006;119:3987–3994. doi:10.1121/1.2197798.
71. Tao C, Zhang Y, Hottinger DG, et al. Asymmetric airflow and vibration induced by the Coanda effect in a symmetric model of the vocal folds. *J Acoust Soc Am*. 2007;122:2270–2278. doi:10.1121/1.2773960.
72. Decker GZ, Thomson SL. Computational simulations of vocal fold vibration: Bernoulli versus Navier-Stokes. *J Voice*. 2007;21:273–284. doi:10.1016/j.jvoice.2005.12.002.
73. Daily DJ, Thomson SL. Acoustically-coupled flow-induced vibration of a computational vocal fold model. *Comput Struct*. 2013;116:50–58. doi:10.1016/j.compstruc.2012.10.022.
74. Šidlof P, Lunéville E, Chambeyron C, et al. Finite element modeling of airflow during phonation. *Journal of Computational and Applied Mechanics*. 2010;4:121–132.
75. Zörner S, Kaltenbacher M. Fluid-structure-acoustic interaction, algorithms and implementations using the finite element method, V European Conference on Computational Fluid Dynamics.
76. Ishizaka K, Matsudaira M. *Fluid Mechanical Considerations of Vocal Cord Vibration*. Santa Barbara, CA: Speech Communication Research Lab; 1972:Monograph 8.
77. Lodermeier A, Becker S, Döllinger M, et al. Phase-locked flow field analysis in a synthetic human larynx model. *Exp Fluids*. 2015;56:doi:10.1007/s00348-015-1942-6.

78. Lodermeier A, Tautz M, Becker S, et al. Aeroacoustic analysis of the human phonation process based on a hybrid acoustic piv approach. *Exp Fluids*. 2018;59:13. doi:10.1007/s00348-017-2469-9.
79. Titze IR. *The Myoelastic Aerodynamic Theory of Phonation*, National Center for Voice and Speech, 2006.
80. Mittal R, Erath B, Plesniak M. Fluid dynamics of human phonation and speech. *Ann Rev Fluid Mech*. 2013;45:437–467. doi:10.1146/annurev-fluid-011212-140636.
81. Durst F. *Fluid Mechanics: An Introduction to the Theory of Fluid Flows*. Berlin, Heidelberg: Springer; 2008. doi:10.1007/978-3-540-71343-2.
82. Kaltenbacher M. *Numerical Simulation of Mechatronic Sensors and Actuators: Finite Elements for Computational Multiphysics*. Berlin, Heidelberg: Springer; 2015. doi:10.1007/978-3-642-40170-1.
83. Donea J, Huerta A, Ponthot J, et al. *Arbitrary Lagrangian-Eulerian Methods*. Encyclopedia of Computational Mechanics. Hoboken: John Wiley & Sons, Ltd; 2004:413–437. doi:10.1002/0470091355.ecm009.
84. Mittal R, Iaccarino G. Immersed boundary methods. *Ann Rev Fluid Mech*. 2005;37:239–261. doi:10.1146/annurev.fluid.37.061903.175743.
85. Renotte C, Bouffieux V, Wilquem F. Numerical 3D analysis of oscillatory flow in the time-varying laryngeal channel. *J Biomech*. 2000;33:1637–1644. doi:10.1016/S0021-9290(00)00134-2.
86. Becker S, Kniesburges S, Müller S, et al. Flow-structure-acoustic interaction in a human voice model. *J Acoust Soc Am*. 2009;125:1351–1361. doi:10.1121/1.3068444.
87. Kniesburges S, Hesselmann C, Becker S, et al. Influence of vortical flow structures on the glottal jet location in the supraglottal region. *J Voice*. 2013;27:531–544. doi:10.1016/j.jvoice.2013.04.005.
88. Kniesburges S, Lodermeier A, Becker S, et al. The mechanisms of subharmonic tone generation in a synthetic larynx model. *J Acoust Soc Am*. 2016;139:3182–3192. doi:10.1121/1.4954264.
89. Kniesburges S, Birk V, Lodermeier A, et al. Effect of the ventricular folds in a synthetic larynx model. *J Biomech*. 2017;55:128–133. doi:10.1016/j.jbiomech.2017.02.021.
90. Neubauer J, Zhang Z, Miraghaie R, et al. Coherent structures of the near field flow in a self-oscillating physical model of the vocal folds. *J Acoust Soc Am*. 2007;121:1102–1118. doi:10.1121/1.2409488.
91. Zhang Z, Neubauer J, Berry D. Influence of vocal fold stiffness and acoustic loading on flow-induced vibration of a single-layer vocal fold model. *J Sound Vib*. 2009;322:299–313. doi:10.1016/j.jsv.2008.11.009.
92. Scherer RC, Shinwari D, Witt KJD, et al. Intraglottal pressure profiles for a symmetric and oblique glottis with a divergence angle of 10 degrees. *J Acoust Soc Am*. 2001;109:1616–1630. doi:10.1121/1.1333420.
93. Kniesburges S. *Fluid-structure-acoustic interaction during phonation in a synthetic larynx model* [PhD dissertation]. Shaker, Aachen, Germany: Friedrich-Alexander University Erlangen-Nürnberg; 2014.
94. Issa RI. Solution of the implicitly discretised fluid flow equations by operator-splitting. *J Comput Phys*. 1986;62:40–65. doi:10.1016/0021-9991(86)90099-9.
95. Nicoud F, Ducros F. Subgrid-scale stress modelling based on the square of the velocity gradient tensor. *Flow Turbul Combust*. 1999;62:183–200. doi:10.1023/A:1009995426001.
96. Lighthill M. On sound generated aerodynamically I. general theory. *Proc R Soc Lond A Math Phys Sci*. 1952;211:564–587. doi:10.1098/rspa.1952.0060.
97. Lighthill M. On sound generated aerodynamically. II. Turbulence as a source of sound. *Proc R Soc Lond A Math Phys Sci*. 1954;222:1–32. doi:10.1098/rspa.1954.0049.
98. Ewert R, Schröder W. Acoustic perturbation equations based on flow decomposition via source filtering. *J Comput Phys*. 2003;188:365–398. doi:10.1016/S0021-9991(03)00168-2.
99. Steger J, Dougherty F, Benek J. A chimera grid scheme [multiple overset body-conforming mesh system for finite difference adaptation to complex aircraft configurations]. In: Ghia KN, Ghia U, eds. *Advances in Grid Generation, Volume ASME FED-5*. 1983:59–69.
100. Khosla S, Oren L, Ying J, et al. Direct simultaneous measurement of intraglottal geometry and velocity fields in excised larynges. *Laryngoscope*. 2014;124:S1–S13. doi:10.1002/lary.24512.
101. Oren L, Khosla S, Gutmark E. Intraglottal pressure distribution computed from empirical velocity data in canine larynx. *J Biomech*. 2014;47:1287–1293. doi:10.1016/j.jbiomech.2014.02.023.
102. Ariff M, Salim S, Cheah S Wall  $y^+$  approach for dealing with turbulent flow over a surface mounted cube: part I, low Reynolds number, Seventh International Conference on CFD in the Minerals and Process Industries.
103. Ferziger J, Peric M. *Computational Methods for Fluid Dynamics*. Berlin, Heidelberg: Springer; 2002. doi:10.1007/978-3-642-56026-2.
104. Triep M, Brücker C. Three-dimensional nature of the glottal jet. *J Acoust Soc Am*. 2010;127:1537–1547. doi:10.1121/1.3299202.
105. Shinwari D, Scherer R, DeWitt K, et al. Flow visualization and pressure distributions in a model of the glottis with a symmetric and oblique divergent angle of 10 degrees. *J Acoust Soc Am*. 2003;113:487–497. doi:10.1121/1.1526468.
106. Triep M, Brücker C, Schröder W. High-speed PIV measurements of the flow downstream of a dynamic mechanical model of the human vocal folds. *Exp Fluids*. 2005;39:232–245. doi:10.1007/s00348-005-1015-3.
107. Erath B, Plesniak M. The occurrence of the Coanda effect in pulsatile flow through static models of the human vocal folds. *J Acoust Soc Am*. 2006;120:1000–1011. doi:10.1121/1.2213522.
108. Drechsel J, Thomson S. Influence of supraglottal structures on the glottal jet exiting a two-layer synthetic, self-oscillating vocal fold model. *J Acoust Soc Am*. 2008;123:4434–4445. doi:10.1121/1.2897040.
109. Xue Q, Zheng X. The effect of false vocal folds on laryngeal flow resistance in a tubular three-dimensional computational laryngeal model. *J Voice*. 2016;31:275–281. doi:10.1016/j.jvoice.2016.04.006.
110. The Regional Computing Center Erlangen (RRZE), online [link]. Available at: <https://www.anleitungen.rrze.fau.de/hpc/emmy-cluster/>. Accessed August 4, 2017.